IEEE Access
Multidisciplinary | Rapid Review | Open Access Journal

Received January 21, 2019, accepted February 7, 2019, date of publication February 12, 2019, date of current version March 4, 2019.

Digital Object Identifier 10.1109/ACCESS.2019.2899038

Design and Analysis of a Long-Stroke Planar Switched Reluctance Motor for Positioning Applications

SU-DAN HUANG[1], (Member, IEEE), GUANG-ZHONG CAO[1], (Senior Member, IEEE), YEPING PENG[1], (Member, IEEE), CHAO WU[1], DELIANG LIANG[2], (Senior Member, IEEE), AND JIANGBIAO HE[3], (Senior Member, IEEE)

[1]Shenzhen Key Laboratory of Electromagnetic Control, College of Mechatronics and Control Engineering, Shenzhen University, Shenzhen 518060, China
[2]State Key Laboratory of Electrical Insulation and Power Equipment, Xi'an Jiaotong University, Xi'an 710049, China
[3]Department of Electrical and Computer Engineering, University of Kentucky, Lexington, KY 40506, USA

Corresponding author: Guang-Zhong Cao (gzcao@szu.edu.cn; gzcao.01@gmail.com)

This work was supported in part by the National Natural Science Foundation of China under Grant NSFC 51677120, Grant NSFC U1813212, and Grant NSFC 51275312, in part by the Natural Science Foundation of Guangdong Province, China, under Grant 2017A030310460 and Grant 2018A030310522, in part by the Shenzhen Government Fund under Grant 20170919104246276, Grant KJYY20160428170944786, and Grant JCYJ20160520175515548, and in part by the Fundamental Research Funds for the Shenzhen University under Grant 2017039.

ABSTRACT This paper presents the design, control, and experimental performance evaluation of a long-stroke planar switched reluctance motor (PSRM) for positioning applications. Based on comprehensive consideration of the electromagnetic and mechanical characteristics of the PSRM, a motor design is first developed to reduce the force ripple and deformation. A control scheme with LuGre friction compensation is then proposed to improve the positioning accuracy of the PSRM. Furthermore, this control scheme is proven to ensure the stable motion of the PSRM system. Additionally, the response speed and steady-state error of the PSRM system with this control scheme are theoretically analyzed. Finally, the experimental results are presented and analyzed. The effectiveness of the precision long-stroke motion of the PSRM and its promise for use in precision positioning applications are verified experimentally.

INDEX TERMS Motion control, planar motor, precision positioning, switched reluctance motor.

I. INTRODUCTION

Precision positioning is playing an increasingly crucial role in various fields, such as semiconductor lithography, microscale manufacturing, and high-precision machining [1], [2]. Conventionally, positioning devices achieve translational motion by means of a rotary motor operating in combination with a mechanical transmission, such as a lead screw and gear [3]. However, such devices inevitably suffer from backlash, stick-slip motion, complicated structures, a need for frequent maintenance, and high costs [4], [5]. Multiple stacked linear motors can also be employed in positioning devices [6], [7]. Despite its simpler structure and lower cost, such a stacked configuration is nevertheless somewhat complex, with a heavy moving mass, low stiffness, and mechanical coupling [8], [9]. These disadvantages may be overcome by using a planar motor. Planar motors achieve translational motion directly through electromagnetic energy, without requiring a mechanical transmission or stacked configuration [10]. Planar motors are simple, with light moving masses, low cost, low friction, high precision, and fewer interfering factors, which are very attractive advantages for precision positioning devices [11], [12].

Planar motors can be categorized into four primary types: variable reluctance, permanent magnet, induction, and direct current (DC) [13], [14]. Regarding variable-reluctance-type planar motors, Sawyer [15] developed a Sawyer motor in 1968, which was the first planar motor, and Pan *et al.* [13] developed the first planar switched reluctance motor (PSRM) in 2005. Several permanent-magnet-type planar motors have also been developed, including the synchronous permanent magnet planar motor designed by Zhang *et al.* in 2013 [14]

The associate editor coordinating the review of this manuscript and approving it for publication was Kan Liu.

and the new planar flux-switching permanent magnet motor designed by Hu *et al.* in 2018 [16]. Regarding induction-type planar motors, Fujii and Fujitake [17] developed such a motor with a toroidal core for two-dimensional motion in 1999, and Treviso *et al.* [18] developed an induction-type planar actuator for surface inspection in 2015. Among DC-type planar motors, Jung and Baek [19] developed a planar motor using direct-drive DC coils and permanent magnets in 2002, and Kou *et al.* [20] developed a Lorentz-force-driven DC planar motor in 2011.

The PSRM is a type of variable-reluctance planar motor that is a promising candidate for use in precision positioning devices by virtue of its various advantages compared to other kinds of planar motors, as listed below [21]–[23].

1) The PSRM is based on the switched reluctance principle and has very few mechanical components; consequently, it has a simple structure and is easy to manufacture.

2) In view of the limited supply of permanent magnets, the PSRM is relatively low in cost and environmentally beneficial.

3) The stroke of the PSRM is simple to extend and, theoretically, can be extended to infinity since the planar dimensions of the stator platform can be easily and infinitely enlarged. Thus, long-stroke motion can be easily realized with the PSRM.

4) The virtually decoupled two-dimensional (2-D) motion and the absence of any positioning error due to a mechanical transmission make the PSRM very suitable for achieving precision positioning.

Long-stroke precision positioning devices are required in specific precision positioning applications [24], [25]. Considerable research has been focused on developing long-stroke planar motors to facilitate industrial precision positioning applications. It has been reported that the Sawyer motor is the only type of planar motor that has been commercialized [26]. H2W Technologies manufactures a commercial air-bearing Sawyer motor with a planar stroke up to 1.0 m $\times$ 1.5 m, which can achieve motion in microsteps of 1 μm [27]. Planar Motor Incorporated manufactures magnetically suspended planar motors with a planar stroke in the centimeter range and a repeatability of 1 μm for conveying systems [28]. Zhu *et al.* [29] developed a magnetically suspended positioner using a permanent magnet planar motor; this positioner had a root-mean-square error of approximately 50 nm for tracking a series of steps of 200 nm. Jung and Baek [19] developed a magnetically suspended planar system employing a DC planar motor that exhibited a repeatable accuracy of approximately 500 nm with a planar stroke of 32 cm $\times$ 32 cm. Pan and Cheung [30] designed a mechanical bearing PSRM that achieved a steady-state error of ± 2 μm for step responses with an amplitude of 20 mm; this PSRM had an actual planar stroke of 100 mm $\times$ 180 mm.

From the work summarized above, it can be concluded that the reported positioning accuracy of contact-type PSRMs is lower than that of the contact-free Sawyer, permanent magnet, and DC planar motors. This is because nonlinear friction is inevitably a major source of positioning error for a contact-type PSRM. From the current state of the art in PSRMs, it is evident that very little research has been performed seeking to eliminate the friction in the existing PSRMs. Additionally, it is challenging to achieve precision motion with a PSRM due to its high nonlinearity and large force ripple. However, this issue can be effectively overcome by adopting an optimal motor design and an effective control strategy.

An effective control strategy for trajectory tracking is an important requirement for motion systems to achieve precision tracking performance [6], [31], [32]. Dulger *et al.* [31], Halicioglu *et al.* [32] designed a proportional-integral-derivative (PID) controller, a cascade feedforward controller, a particle swarm optimization-based neural network controller, a back-propagation controller, and other controllers for servo systems to achieve high tracking performance. In addition to these controllers, a compensation control method has been proposed to improve tracking performance [33]. Yao *et al.* [34] proposed a LuGre-model-based friction compensation method for hydraulic actuators with the goal of effectively eliminating friction to achieve precision tracking performance. Such an effective friction compensation control strategy is an attractive means of improving the motion precision of contact-type PSRMs.

This paper presents a long-stroke contact-type PSRM that is designed to achieve higher positioning accuracy for positioning applications. A motor design is presented and analyzed considering both electromagnetic and mechanical performances. Then, a control scheme with nonlinear friction compensation to eliminate the negative effects of friction is proposed and analyzed; this scheme is the first of its kind for PSRMs. Finally, experimental results are reported and analyzed. The main contributions of this study with respect to the PSRMs reported to date are 1) the application of nonlinear LuGre friction compensation to eliminate the negative effects of friction to achieve higher positioning accuracy and 2) a demonstration of precision positioning performance for a long-stroke PSRM with mechanical bearings, illustrating the promising possibility to achieve higher positioning performance for precision positioning applications using contactless bearings.

II. MOTOR DESIGN

A PSRM is designed on the basis of the previous PSRM design presented in [30] for precision long-stroke positioning. Fig. 1 shows the overall structure and the developed prototype of the designed PSRM.

A. STATOR AND MOVER DESIGN

1) SELECTION OF THE DIMENSIONS

Consider a PSRM to be designed with a maximum single-phase thrust force f_{max} of 32 N, a maximum velocity v_{max} of 1 m/s, and a maximum single-phase current of 10 A. Under the assumption of zero friction, the maximum power

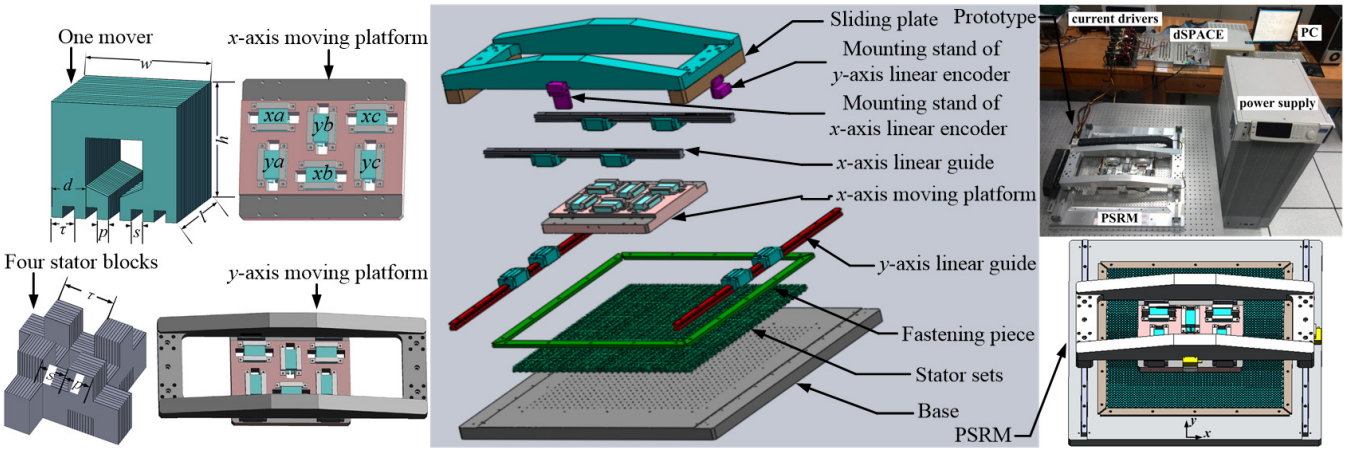

FIGURE 1. Overall structure and developed prototype of the designed PSRM.

capacity of one axis is

$$P_{\max} = f_{\max} v_{\max} \tag{1}$$

The pole pitch of the stator and mover is expressed as

$$\tau = p + s \tag{2}$$

where p is the tooth width and s is the slot width.

The mover width is represented by

$$w = n\tau - s \tag{3}$$

where n is the number of tooth pairs per mover.

The cross-sectional area of the air gap at the aligned position between the stator and mover is given by

$$A_g = npl_m\sigma(1+\sigma)^{-1} \tag{4}$$

where l_m is the stack length of the mover and σ is given by

$$\sigma = ps^{-1} \tag{5}$$

If the flux leakage is neglected, the flux linkage at the aligned position can be expressed as

$$L_a i = B_g A_g N \tag{6}$$

where L_a is the phase inductance at the aligned position, i is the phase current, B_g is the average magnetic flux density in the air gap, and N is the number of turns per phase.

At the maximum velocity, the change in the flux linkage from the aligned position to the unaligned position is given by

$$\Delta\psi = (L_a - L_u)i = L_a(1-\lambda^{-1})i = u\Delta t \tag{7}$$

where L_u is the phase inductance at the unaligned position, u is the phase voltage, $\lambda = L_a/L_u$, and t is the time interval over which the mover moves from the aligned position to the unaligned position.

t is represented by

$$\Delta t = 0.5\tau v_{\max}^{-1} \tag{8}$$

By combining (6) and (7), the phase voltage is derived to be

$$u = 2\tau^{-1} v_{\max}(1-\lambda^{-1}) B_g A_g N. \tag{9}$$

The maximum power capacity of one axis is [35]

$$P_{\max} = K_e K_d u i = K_e K_d K_1 K_2 A_g B_g v_{\max} A \tag{10}$$

where $K_1 = 2(n+n\sigma--1)/(1+\sigma)$, $K_2 = 1–\lambda^{-1}$, K_d is the duty cycle of the motor, which is determined by the current conduction position for each rising inductance profile, K_e is the efficiency of the motor, which is usually in the range of [0.65, 0.75] [35]; and A is the specific electric loading of the mover, expressed in ampere conductors per meter.

A usually ranges from 25000 to 90000 A/m [36] and is represented by

$$A = Niw^{-1}. \tag{11}$$

By combining (1), (10), and (11), the cross-sectional area of the air gap can be expressed as

$$A_g = f_{\max} v_{\max}(K_e K_d K_1 K_2 B_g v_{\max} N i w^{-1})^{-1}. \tag{12}$$

From (4) and (12), the stack length of the mover is

$$l_m = f_{\max} v_{\max} w(1+\sigma)(K_e K_d K_1 K_2 B_g v_{\max} N i \sigma np)^{-1}. \tag{13}$$

On the basis of Ampere's circuital law, the number of turns per phase is derived to be

$$N = (H_a l_a + 2gB_g\mu_0^{-1})i^{-1} \tag{14}$$

where H_a, μ_0, l_a, and g are the average magnetic field strength in the silicon steel, the permeability of air, the average length of the magnetic path along the stator and mover, and the length of the air gap, respectively.

2) DETERMINATION OF THE DIMENSIONS

The length of the air gap should be as small as possible to maximize the average force while respecting the manufacturing tolerance [37]. The length of the air gap is therefore selected to be $g = 0.3$ mm. Regarding the specific velocity,

a smaller pole pitch leads to a shorter motion period, resulting in a decreased force ripple. A smaller pole pitch also leads to a smaller thrust force. In addition, to ensure that the three-phase movers are evenly distributed at positions within the pole pitch, the pole pitch should be a multiple of 3. Hence, the pole pitch is chosen to be $\tau = 7.2$ mm instead of the pole pitch of 9 mm chosen for the previous PSRM. Regarding the specific volume of the motor, the distribution of the force on each tooth of each mover becomes more uniform as the number of tooth pairs per mover increases, resulting in a reduced force ripple. However, increasing the number of tooth pairs per mover increases the complexity of the structure and makes manufacturing more complicated.

The number of tooth pairs per mover is thus selected to be $n = 3$ instead of $n = 2$, as in the previous PSRM.

From (2), the tooth width and slot width are calculated to be $p = 3.6$ mm and $s = 3.6$ mm, respectively. From (3), the mover width is calculated to be $w = 39.6$ mm. The mover height is reasonably selected to be $h = 36.0$ mm. Accordingly, the average length of the magnetic path along the stator and mover can be derived to be $l_a = 145.1$ mm. On the basis of the B-H characteristics of the silicon steel and the air gap under the maximum current, the average magnetic flux density in the air gap and the average magnetic field strength in the silicon steel are selected to be $B_g = 1.5$ T and $H_a = 5000$ A/m, respectively. The parameters K_e and K_d are set to be $K_e = 0.7$ and $K_d = 1$, respectively. From (14), the number of turns per phase is calculated to be $N = 145$ turns. Additionally, the stack length of the mover is deduced to be $l_m = 42.3$ mm from (13).

Based on the determined dimensions of the stator and mover, a three-dimensional static finite element model (FEM) of the stator sets and three-phase movers on one axis was established using ANSYS® software. A certain phase was energized by a constant current for several current values in intervals of 1 A. For each constant current, the single-phase thrust force and normal force were calculated at various positions under a pole pitch of 7.2 mm using the finite element method. The single-phase thrust force and normal force are plotted versus the current, which ranges from 1 to 10 A, and versus the position, which ranges from 0 to 7.2 mm, in Figs. 2(a) and 2(b), respectively. The maximum thrust force and maximum normal force are 34.1 and 380.1 N, respectively, for single-phase excitation. Hence, the generated thrust force satisfies the design requirement of a maximum thrust force of 32 N.

B. MOVING PLATFORMS DESIGN

The geometry of the moving platforms is designed to reduce the platform deformation compared with the previous PSRM. Because the largest deformation occurs on the *y*-axis moving platform, this platform is the main focus of the design.

Using the finite element method based on ANSYS®, a static structural analysis of the moving platforms was performed under the most extreme conditions, in which four normal forces of 400 N, slightly larger than the maximum

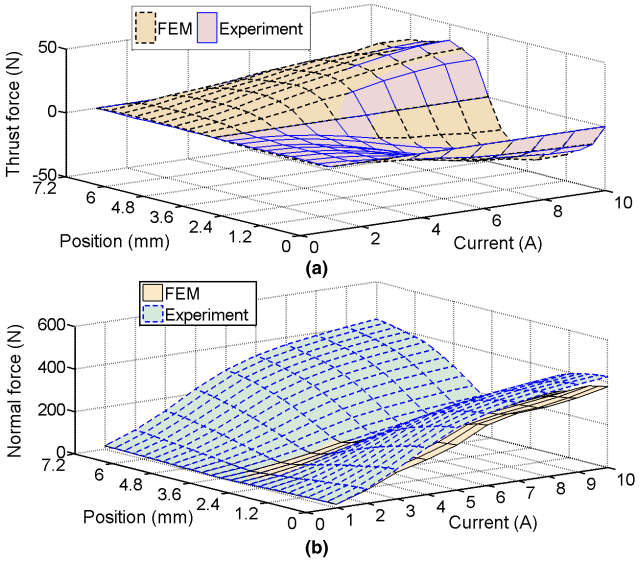

FIGURE 2. (a) Thrust force and (b) normal force of the PSRM obtained from FEM and experimental measurement.

normal force, act on four movers, since the maximum number of excited phases is two on each axis.

The dimensions of the *x*-axis moving platform in the previous design are indicated in Fig. 3(a). Fig. 3(b) presents the dimensions of the newly designed *x*-axis moving platform, which has a mass of 5.7 kg. Under the most extreme conditions, the maximum deformation of the previous platform is 0.01612 mm, whereas the maximum deformation of the newly designed platform is 0.00405 mm, corresponding to a reduction of 74.9%.

Fig. 3(c) shows the dimensions of the sliding plate of the *y*-axis moving platform in the previous design. The dimensions of the newly designed sliding plate of the *y*-axis moving platform are presented in Fig. 3(d). An enhanced stiffening rib is applied, reducing the maximum sliding plate deformation from 0.12636 mm for the previous platform to 0.03418 mm for the newly designed platform, a decrease of 72.5%.

Under single-phase excitation, the theoretical maximum velocities of the *x*- and *y*-axes are 1.01 and 0.89 m/s, respectively. The maximum velocity is thus higher than 1.01 m/s under two-phase excitation. The designed moving platforms satisfy the requirement of a maximum velocity of 1 m/s.

III. CONTROL STRATEGY

A. CONTROL SCHEME

Fig. 4 shows the block diagram of the proposed PSRM control scheme. Nonlinear friction estimation is introduced into the conventional 2-D motion control scheme; the estimated friction is used to counteract the actual friction, and thus, the position error caused by friction can be effectively eliminated by means of suitable control action. For the l-axis ($l = x$ or y) of the PSRM, e_l is the position error between the desired position p_{l_ref} and the detected position p_l($p_l \approx$ actual positionp_{l_real}); u_{l_c} is the thrust force command; f^{*l_f} is the estimated friction; f_l^* is the

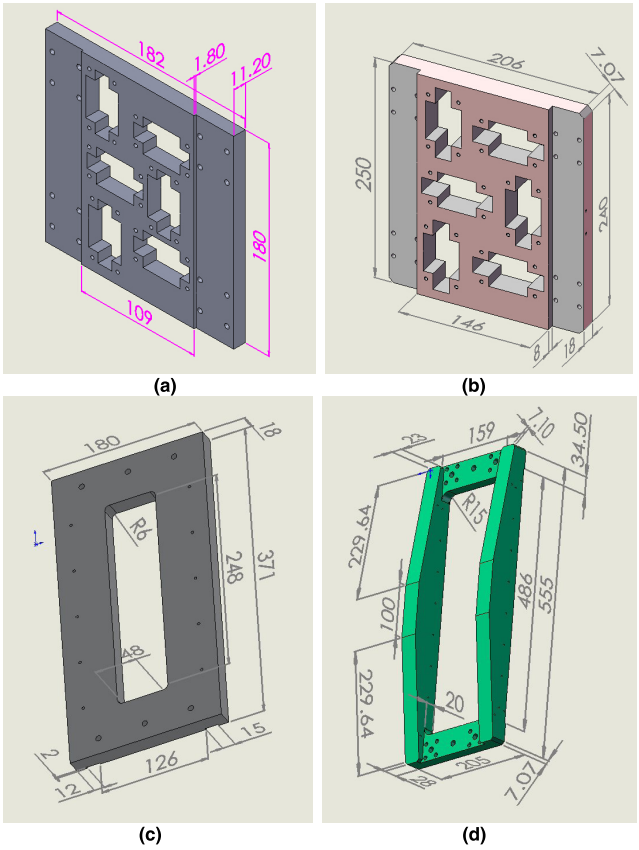

FIGURE 3. Dimensions of (a) the previous designed *x*-axis moving platform, (b) newly designed *x*-axis moving platform, (c) previous designed sliding plate, and (d) newly designed sliding plate.

desired thrust force; $f^*_{l\_a}$, $f^*_{l\_b}$, and $f^*_{l\_c}$ are the desired three-phase thrust forces; $i^*_{l\_a}$, $i^*_{l\_b}$, and $i^*_{l\_c}$ are the desired three-phase currents; and i_{l_a}, i_{l_b}, and i_{l_c} are the detected three-phase currents.

A proportional-derivative (PD) position controller is used to issue the thrust force command to the PSRM system. The control law of the controller, i.e., the thrust force command, is

$$u_{l\_c} = k_{l\_p} e_l + k_{l\_d} \dot{e}_l \tag{15}$$

where $k_{l\_p} > 0$ and $k_{l\_d} > 0$ are the proportional and derivative parameters, respectively, of the PD controller.

B. NONLINEAR FRICTION COMPENSATION

The l-axis mechanical movement can be expressed as

$$M_l \ddot{p}_l = f_l - f_{l\_f} - f_{l\_d} \tag{16}$$

where M_l, p_l, f_l, f_{l_f}, and f_{l_d} are the mass of the moving platform, the position, the thrust force, the friction, and the external load force, respectively, on the l-axis.

The desired thrust force f_l^* consists of two components, namely, a thrust force command u_{l_c} and an estimated friction $f^*_{l\_f}$, it is expressed as

$$f_l^* = u_{l\_c} + f^*_{l\_f}. \tag{17}$$

By substituting (17) into (16) and neglecting the external load force, the mechanical movement equation can be written as

$$M_l \ddot{p}_l = u_{l\_c} + f^*_{l\_f} - f_{l\_f}. \tag{18}$$

If the friction is estimated very accurately, i.e., $f^*_{l\_f} \approx f_{l\_f}$, then the PSRM will behave like a frictionless motor, meaning that the l-axis transfer function can be expressed as

$$G_l(s) = \frac{k}{M_l s^2} \tag{19}$$

where k is a constant coefficient.

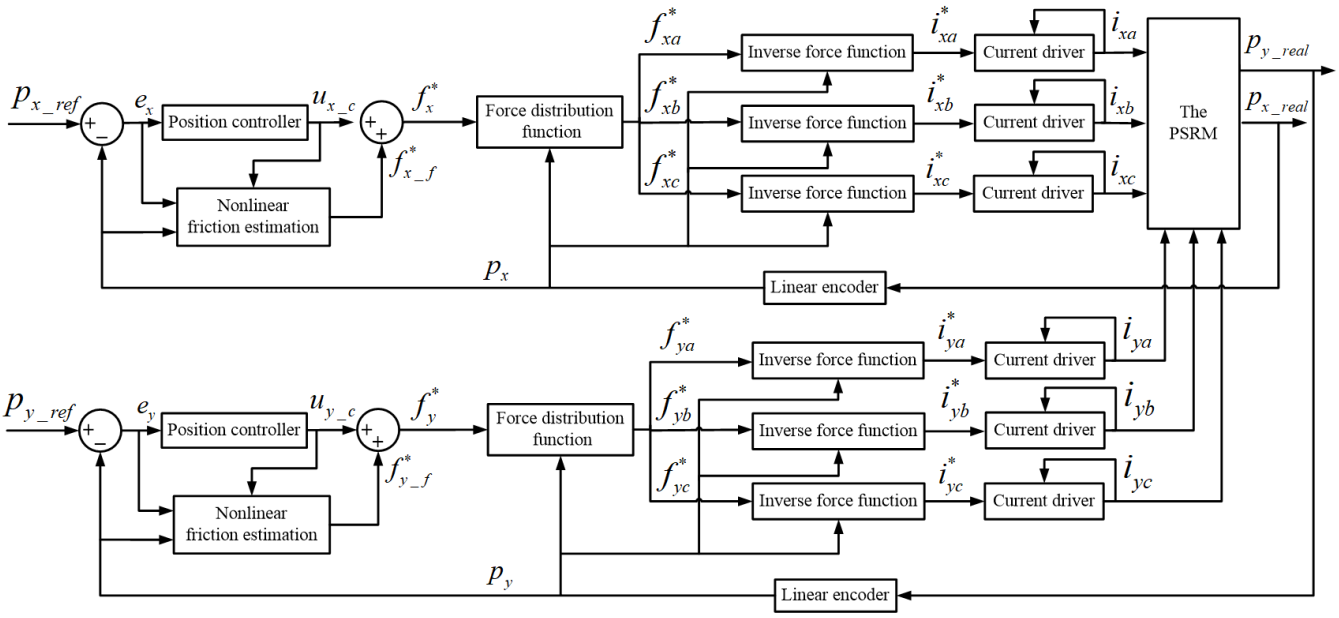

FIGURE 4. Block diagram of the proposed PSRM control scheme.

The LuGre friction model [33], [34] is applied to represent the nonlinear friction of the PSRM. Thus, the l-axis friction is given by

$$f_{l\_\mathrm{f}} = \sigma_{l\_0} z_l + \sigma_{l\_1} \dot{z}_l + \sigma_{l\_2} \dot{p}_l \tag{20}$$

$$\dot{z}_l = \dot{p}_l - \frac{|\dot{p}_l|}{g(\dot{p}_l)} z_l \tag{21}$$

$$g(\dot{p}_l) = \frac{1}{\sigma_{l\_0}} \left(f_{l\_\mathrm{c}} + \left(f_{l\_\mathrm{s}} - f_{l\_\mathrm{c}} \right) e^{-\left(\dot{p}_l v_{l\_s}^{-1} \right)^2} \right) \tag{22}$$

where σ_{l_0}, σ_{l_1}, and σ_{l_2} are the friction parameters on the l-axis; z_l is the l-axis internal friction state which cannot be directly measured by sensors; f_{l_s} is the l-axis stiction force; f_{l_c} is the l-axis Coulomb friction; v_{l_s} is the l-axis Stribeck velocity; and (22) is greater than zero.

The estimated friction $f_{l\_\mathrm{f}}^*$ is given by

$$f_{l\_\mathrm{f}}^* = \sigma_{l\_0} z_l^* + \sigma_{l\_1} \dot{z}_l^* + \sigma_{l\_2} \dot{p}_l \tag{23}$$

$$\dot{z}_l^* = \dot{p}_l - \frac{|\dot{p}_l|}{g(\dot{p}_l)} z_l^* + K_l \tag{24}$$

where z_l^* is the estimated l-axis internal friction state and K_l is the l-axis adaptive regulation term for the estimation.

By using Lyapunov stability theory, the adaptive regulation term K_l of the proposed control scheme is deduced to be

$$K_l = \frac{u_{l\_\mathrm{c}} \left(M_l \ddot{p}_l - u_{l\_\mathrm{c}} \right)}{\sigma_{l\_1} u_{l\_\mathrm{c}} + e_l k_{l\_\mathrm{d}} \left(\frac{\sigma_{l\_1} |\dot{p}_l|}{g(\dot{p}_l)} - \sigma_{l\_0} \right)}. \tag{25}$$

C. STABILITY ANALYSIS

By substituting (20) and (23) into (16) and combining (21), (22), and (24), the mechanical movement equation can be rewritten as

$$M_l \ddot{p}_l = u_{l\_\mathrm{c}} - \sigma_{l\_0} e_{l\_\mathrm{z}} + \frac{\sigma_{l\_1} |\dot{p}_l|}{g(\dot{p}_l)} e_{l\_\mathrm{z}} + \sigma_{l\_1} K_l \tag{26}$$

where e_{l_z} is the error on the internal friction state and is given by

$$e_{l\_\mathrm{z}} = z_l - z_l^*. \tag{27}$$

From (26), the error on the internal friction state is derived to be

$$e_{l\_\mathrm{z}} = \frac{M_l \ddot{p}_l - u_{l\_\mathrm{c}} - \sigma_{l\_1} K_l}{\frac{\sigma_{l\_1} |\dot{p}_l|}{g(\dot{p}_l)} - \sigma_{l\_0}}, \quad \frac{\sigma_{l\_1} |\dot{p}_l|}{g(\dot{p}_l)} \neq \sigma_{l\_0}. \tag{28}$$

When $\sigma_{l\_1} |\dot{p}_l| / g(\dot{p}_l) = \sigma_{l\_0}$, let $\sigma_{l\_0} = \sigma_{l\_0} + \rho$ (where ρ is a parameter with a very small value), such that, $\sigma_{l\_1} |\dot{p}_l| / g(\dot{p}_l) \neq \sigma_{l\_0}$ for all operating condition.

By subtracting (24) from (21), the derivative of e_{l_z} is found to be

$$\dot{e}_{l\_\mathrm{z}} = -\frac{|\dot{p}_l|}{g(\dot{p}_l)} e_{l\_\mathrm{z}} - K_l. \tag{29}$$

A function is defined for the PSRM control system as follows:

$$F\left(e_l, e_{l\_\mathrm{z}}\right) = \frac{1}{2} e_l^2 e_{l\_\mathrm{z}}^2. \tag{30}$$

The derivative of the function F is deduced to be

$$\begin{aligned} \dot{F}(e_l, e_{l\_\mathrm{z}}) &= e_l \dot{e}_l e_{l\_\mathrm{z}}^2 + e_l^2 e_{l\_\mathrm{z}} \dot{e}_{l\_\mathrm{z}} \\ &= e_l e_{l\_\mathrm{z}}^2 \left(\frac{u_{l\_\mathrm{c}}}{k_{l\_\mathrm{d}}} - \frac{k_{l\_\mathrm{p}}}{k_{l\_\mathrm{d}}} e_l \right) + e_l^2 e_{l\_\mathrm{z}} \left(-\frac{|\dot{p}_l|}{g(\dot{p}_l)} e_{l\_\mathrm{z}} - K_l \right) \\ &= -\left(\frac{k_{l\_\mathrm{p}}}{k_{l\_\mathrm{d}}} + \frac{|\dot{p}_l|}{g(\dot{p}_l)} \right) e_l^2 e_{l\_\mathrm{z}}^2 + \frac{u_{l\_\mathrm{c}}}{k_{l\_\mathrm{d}}} e_l e_{l\_\mathrm{z}}^2 - K_l e_l^2 e_{l\_\mathrm{z}}. \end{aligned} \tag{31}$$

For $k_{l\_\mathrm{p}} > 0$, $k_{l\_\mathrm{d}} > 0$, $g(\dot{p}_l) > 0$, and K_l as formulated in (25), the derivative of the function F is

$$\dot{F}\left(e_l, e_{l\_\mathrm{z}}\right) = -\left(\frac{k_{l\_\mathrm{p}}}{k_{l\_\mathrm{d}}} + \frac{|\dot{p}_l|}{g(\dot{p}_l)} \right) e_l^2 e_{l\_\mathrm{z}}^2 \leq 0. \tag{32}$$

Under the condition of $e_l = 0$, according to (25), the adaptive regulation term K_l can be expressed as

$$K_l = \frac{M_l \ddot{p}_l - u_{l\_\mathrm{c}}}{\sigma_{l\_1}}. \tag{33}$$

Then, from (28), e_{l_z} is derived to be

$$e_{l\_\mathrm{z}} = 0. \tag{34}$$

Under the condition of $e_{l\_\mathrm{z}} = 0$, according to (26), the adaptive regulation term K_l can be expressed as shown in (33); then, from (25), e_l is derived to be

$$e_l k_{l\_\mathrm{d}} \left(\frac{\sigma_{l\_1} |\dot{p}_l|}{g(\dot{p}_l)} - \sigma_{l\_0} \right) = 0. \tag{35}$$

Since $\sigma_{l\_1} |\dot{p}_l| / g(\dot{p}_l) \neq \sigma_{l\_0}$,

$$e_l = 0. \tag{36}$$

Therefore, if $e_l = 0$, then $e_{l\_\mathrm{z}} = 0$, and if $e_{l\_\mathrm{z}} = 0$, then $e_l = 0$. Let $\beta = e_l e_{l\_\mathrm{z}}$; then, $\beta = 0$ only under the condition that $e_l = 0$ and $e_{l\_\mathrm{z}} = 0$, i.e., $\beta \to 0$ as $e_l \to 0$ and $e_{l\_\mathrm{z}} \to 0$.

A positive-definite function is defined for the PSRM control system as follows:

$$V(\beta) = \frac{1}{2} \beta^2. \tag{37}$$

According to (30), (32), and (37), the derivative of the positive-definite function V is

$$\dot{V}(\beta) = -\left(\frac{k_{l\_\mathrm{p}}}{k_{l\_\mathrm{d}}} + \frac{|\dot{p}_l|}{g(\dot{p}_l)} \right) \beta^2 \leq 0. \tag{38}$$

According to the Lyapunov global asymptotic stability theorem, every trajectory $\beta(t)$ converges to zero as $t \to 0$ for the following reasons: 1) $V(\beta)$ is positive definite and 2) $\dot{V}(\beta) < 0$ for all $\beta \neq 0$ and $\dot{V}(0) = 0$. Since $\beta \to 0$ as $e_l \to 0$ and $e_{l\_\mathrm{z}} \to 0$, the PSRM system is globally asymptotically stable.

D. ANALYSIS OF CONTROL PERFORMANCE

For $k_{l\_\mathrm{p}} > 0$, $k_{l\_\mathrm{d}} > 0$, and K_l as given in (25), the PSRM system is stable with the proposed control scheme; the l-axis transfer function of the stable PSRM system can be approximately described as shown in (19).

1) SPEED OF RESPONSE

The crossover frequency of the l-axis open loop transfer function of the stable PSRM system is

$$\omega_{l\_c}(s) = \left(\frac{k^2 k_{l\_d}^2 + \sqrt{k^4 k_{l\_d}^4 + 4M_l^2 k^2 k_{l\_p}^2}}{2M_l^2} \right)^{\frac{1}{2}}. \quad (39)$$

The crossover frequency ω_{l_c} of the open-loop transfer function is proportional to the bandwidth frequency of the closed-loop transfer function, which is proportional to the speed of the response. From (39), it can be concluded that the mass M_l of the l-axis moving platform is inversely proportional to the response speed.

E. STEADY STATE ERROR

By using the static error coefficient method, it can be seen that as time approaches infinity, the l-axis steady-state errors of the stable PSRM system for step, ramp, and acceleration inputs theoretically approach

$$e_{l\_ss} = \begin{cases} 0, & \text{for } p_{l\_ref} = R \neq 0 \\ 0, & \text{for } p_{l\_ref} = Rt \\ \dfrac{2M_l R}{k k_{l\_p}}, & \text{for } p_{l\_ref} = Rt^2 \end{cases} \quad (40)$$

The l-axis steady-state error of the stable PSRM system with respect to a sinusoidal input can be derived to be

$$e_{l\_ss} = A_m \sin(\omega t + \theta), \quad \text{for } p_{l\_ref} = B_m \sin(\omega t) \quad (41)$$

where $\omega > 0$, $B_m > 0$, and A_m and θ are given by

$$A_m = \frac{M_l \omega^2 B_m}{\sqrt{\left(M_l \omega^2 - k k_{l\_p}\right)^2 + \omega^2 k^2 k_{l\_d}^2}},$$
$$\theta = \arctan\left(\frac{\omega k k_{l\_d}}{M_l \omega^2 - k k_{l\_p}} \right). \quad (42)$$

As seen from (40) to (42), a larger M_l leads to a larger steady-state error; in addition, larger R and B_m values result in a larger steady-state error. Thus, the steady-state error of a lighter moving platform is generally smaller than that of a heavier one, and a longer stroke results in a larger steady-state error. It can be concluded that high precision and a long stroke are difficult to achieve simultaneously for the motion of the PSRM.

IV. EXPERIMENTAL RESULTS AND DISCUSSION

A. EXPERIMENTAL RESULTS

An experimental setup for testing the PSRM control system was established as shown in Fig. 1. Two Renishaw®TONIC™ high-precision linear optical encoders with a resolution of 50 nm were used to detect x- and y-axis positions. Six Advanced Motion Controls® 50A20 PWM (pulse width modulation) servo drives were employed to provide DC currents to energize six-phase windings. dSPACE® modular hardware was also applied in the system, including a DS1005 PPC (PowerPC) board with a PowerPC 750GX processor running at 1 GHz, a DS3001 incremental encoder interface board with a maximum input frequency of 1.25 MHz, a DS2003 A/D (analogue-to-digital converter) board, and a DS2103 D/A (digital-to-analogue converter) board. The control algorithm was developed based on MATLAB®/Simulink software and was downloaded to the dSPACE® modular hardware to implement real-time control. The sampling time of the control algorithm was 0.5 ms. In (19), $k = 1000$ mm/m, $M_x = 5.9$ kg, and $M_y = 13.9$ kg.

Figs. 2(a) and 2(b) depict the experimentally measured single-phase thrust force and normal force of the PSRM. The mean relative errors between the experimental and FEM values of the thrust force and normal force are in the ranges of [0.03%, 11.11%] and [0.65%, 2.82%], respectively. For the thrust force, the mean relative errors are 11.11% at the aligned and unaligned positions and are less than 1.89% at other positions. At the aligned and unaligned positions, the theoretical thrust force is 0 N, whereas the measured thrust force is a near-zero value with some measurement uncertainty. Thus, the mean relative errors on the thrust force are slightly large at the aligned and unaligned positions. As seen from Fig. 2, the experimentally measured thrust force and normal force coincide with the FEM results.

As seen from Fig. 2, the amplitudes of the single-phase thrust force and normal force are in the ranges of [0, 38.4] and [0, 427.4] N, respectively. The amplitude of the thrust force for two-phase excitation lies in the range of [0, 43.1] N. Therefore, the theoretical maximum x- and y-axis accelerations are 7.31 and 3.10 m/s2, respectively, and the theoretical maximum velocities of the x- and y-axes are 1.58 and 1.34 m/s, respectively.

For various types of uniform motion of the PSRM control system on the l-axis, the velocities and friction forces without friction compensation were experimentally estimated; using these estimated velocities and friction forces, the parameters f_{l_c},f_{l_s}, v_{l_s}, and σ_{l_2} were identified via curve fitting and the method of least squares. For motionless operation of the PSRM open-loop system on the l-axis under a ramp signal with a reference thrust force that was less than the stiction force f_{l_s}, the preparatory displacement without friction compensation was experimentally estimated; using the estimated preparatory displacement, the parameters σ_{l_0} and σ_{l_1} were estimated using curve fitting and the method of least squares. Then, an l-axis LuGre friction model was built using the estimated parameters f_{l_c}, f_{l_s}, v_{l_s}, σ_{l_0}, σ_{l_1}, and σ_{l_2}. According to the experimental results, the estimated x-axis friction can be expressed as

$$f_{x_f}^* = 118913.2532 z_x^* + 1162.3000 \dot{z}_x^* + 10.3128 \dot{p}_x \quad (43)$$
$$\dot{z}_x^* = \dot{p}_x - \frac{|\dot{p}_l|}{g(\dot{p}_x)} z_x^* + K_x \quad (44)$$
$$g(\dot{p}_x) = \frac{1}{118913.2532} \times \left[0.2399 + (3.5908 - 0.2399) e^{-\left(\frac{\dot{p}_x}{0.0436}\right)^2} \right] \quad (45)$$

where the x-axis stiction force and the x-axis Coulomb friction are 3.5908 and 0.2399 N, respectively.

The estimated y-axis nonlinear friction is given by

$$f_{y\mathrm{f}}^{*} = 84737 z_{y}^{*} + 1493.5 \dot{z}_{y}^{*} + 25.8778 \dot{p}_{y} \tag{46}$$

$$\dot{z}_{y}^{*} = \dot{p}_{y} - \frac{|\dot{p}_{y}|}{g\left(\dot{p}_{y}\right)} z_{y}^{*} + K_{y} \tag{47}$$

$$g(\dot{p}_{y}) = \frac{1}{84737} \times \left[0.8179 + (4.3917 - 0.8179) e^{-\left(\frac{\dot{p}_{y}}{0.0222}\right)^{2}}\right] \tag{48}$$

where the y-axis stiction force and the y-axis Coulomb friction are 4.3917 and 0.8179 N, respectively.

Using the PSRM control system, a tracking test for a circular trajectory with a radius of 15 mm was performed with and without nonlinear friction compensation. The x- and y-axis tracking errors are presented in Fig. 5. At the 90 s time point, nonlinear friction compensation began to be applied to the system. Without nonlinear friction compensation, the x- and y-axis tracking errors are within $\pm$20.5 and $\pm$17.4 μm, respectively. With nonlinear friction compensation, the x- and y-axis tracking errors are within $\pm$10.4 and $\pm$11.6 μm, respectively. From Section III-D, it is apparent that the steady-state error of the lighter, x-axis platform is generally smaller than that of the heavier, y-axis platform. Hence, these results are consistent with the control performance analysis. The nonlinear friction compensation reduces the x- and y-axis tracking errors by 49.3% and 33.3%, respectively. These results demonstrate the effectiveness of the PSRM system with the proposed control scheme.

To verify the positioning accuracy of the PSRM system with the proposed scheme, point-to-point trajectory tracking and continuous trajectory tracking tests were performed. The current command and thrust force command were limited to 10 A and 40 N, respectively. Based on the position detected by the linear optical encoder, the velocity and acceleration were estimated via numerical differentiation. The PD control parameters are listed in Table I. For tracking different trajectories, an optimization simulation of the PSRM control system with the PD controller was built to identify the optimal k_{l_p} and k_{l_d} values using a simplex algorithm based on MATLAB®/Simulink. The obtained optimal k_{l_p} and k_{l_d} values were then applied in the actual PSRM control system. The k_{l_p} and k_{l_d} values listed in Table I are those obtained after correction during the experiment to achieve satisfactory control performance.

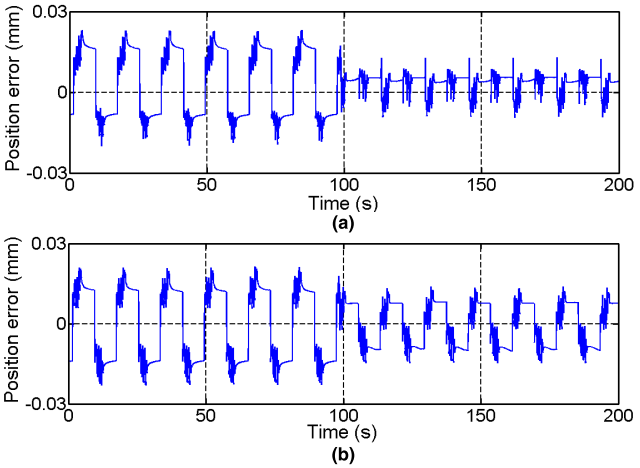

FIGURE 5. (a) x- and (b) y-axes tracking errors of the PSRM system with and without nonlinear friction compensation.

Fig. 6 shows the response for a trapezoidal trajectory with a maximum travel range of 290 mm for the y-axis, where $k_{y\_\mathrm{p}} = 987.0$ and $k_{y\_\mathrm{d}} = 1.60$. The response for a staircase trajectory with a step size of 50 mm is depicted in Fig. 7 for the y-axis, where $k_{y\_\mathrm{p}} = 800.0$ and $k_{y\_\mathrm{d}} = 1.23$. For both motions on the y-axis, the steady-state errors are within $\pm$1.6 μm; the observed velocities and accelerations are in the ranges of [−0.14, 0.15] m/s and [−3.06, 1.66] m/s2, respectively. The observed velocities and accelerations are smaller than their theoretical maximum values.

Planar motions were implemented for tracking a rhombic trajectory and a pentagonal trajectory, as shown in Fig. 8. For the rhombic trajectory, $k_{x\_\mathrm{p}} = 400.0$, $k_{x\_\mathrm{d}} = 1.48$, $k_{y\_\mathrm{p}} = 501.6$, and $k_{y\_\mathrm{d}} = 1.57$. For the pentagonal trajectory, $k_{x\_\mathrm{p}} = 200.3$, $k_{x\_\mathrm{d}} = 1.53$, $k_{y\_\mathrm{p}} = 280.5$, and $k_{y\_\mathrm{d}} = 1.08$. For both motions, the frequency was 1/3 Hz. For the rhombic and pentagonal trajectories, the tracking errors are within $\pm$18.2 and $\pm$56.8 μm, respectively; again, the observed velocities and accelerations are smaller than their theoretical maximum values.

B. DISCUSSION

For the PSRM, the steady-state error is 1.5 μm for translational motion with a travel range of 290 mm, and the

TABLE 1. Parameters of the PD control and position error of the PSRM system.

Trajectory tracking	k_{x_p}	k_{x_d}	k_{y_p}	k_{y_d}	Steady state error	x-axis tracking error	y-axis tracking error
x-axis staircase of 0.5-μm step size	3200.0	1.50	—	—	±0.4 μm	—	—
y-axis staircase of 0.5-μm step size	—	—	6000.0	3.00	±0.4 μm	—	—
y-axis staircase of 50-mm step size	—	—	800.0	1.23	±1.6 μm	—	—
y-axis trapezoid of 290-mm travel range	—	—	987.0	1.60	±1.5 μm	—	—
Rhombus of 60.00-mm travel range	400.0	1.48	501.6	1.57	—	[–14.2, 14.3] μm	[–18.2, 16.9] μm
Pentagram of 57.06-mm travel range	200.3	1.53	280.5	1.08	—	[–31.5, 38.6] μm	[–52.7, 56.8] μm

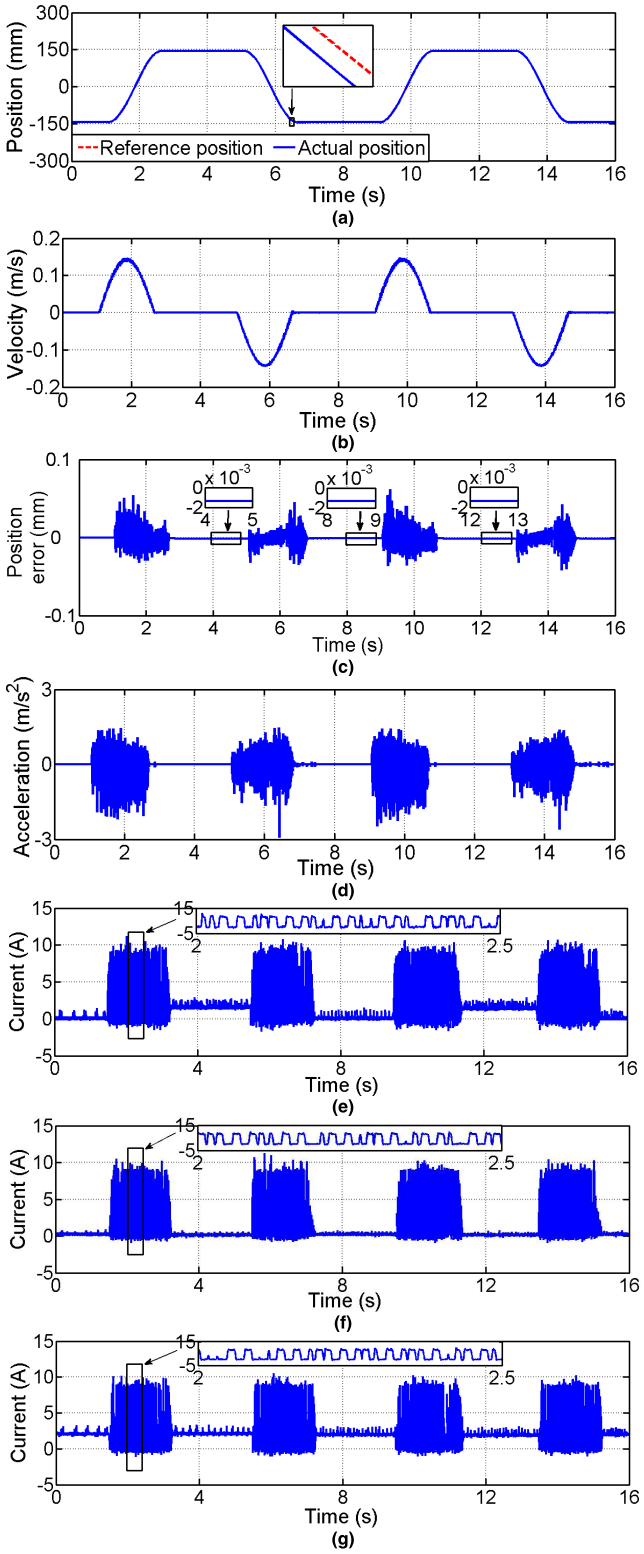

FIGURE 6. (a) Position trajectory, (b) velocity, (c) position error, (d) acceleration, (e) i_{xa}, (f) i_{xb}, and (g) i_{xc} for trapezoid-trajectory responses with a travel range of 290 mm.

tracking error is within ± 56.8 μm for continuous trajectory tracking with a motion range within 60 mm. For comparison, the steady-state error of the previous PSRM reported

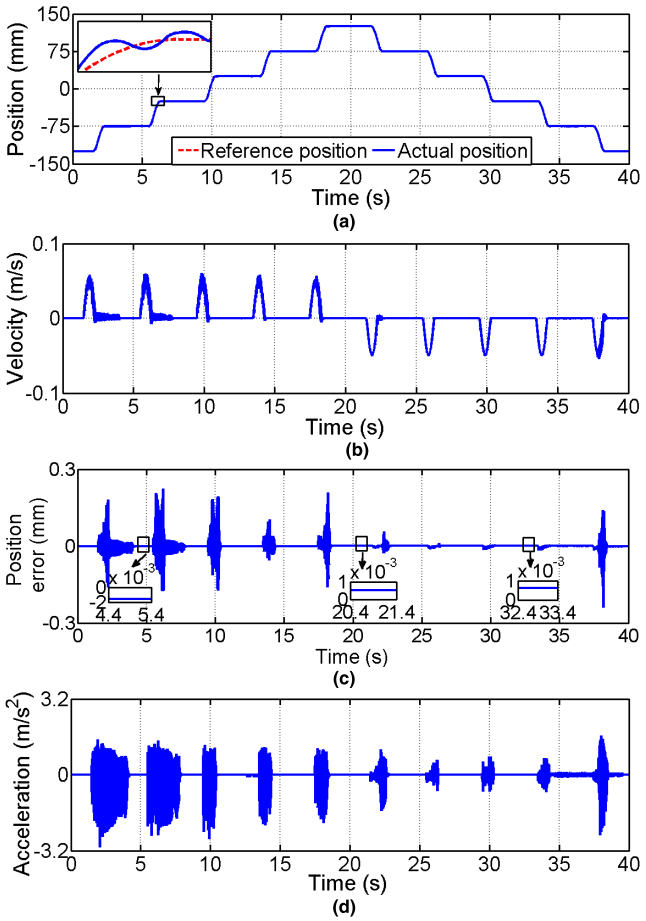

FIGURE 7. (a) Position trajectory, (b) velocity, (c) position error, and (d) acceleration for staircase-trajectory responses with a step size of 50 mm.

in [26] is within ± 2 μm for translational motion with a travel range of 20 mm, and the tracking error of the previous PSRM reported in [16] is within ± 500 μm for continuous trajectory tracking within a motion range of 40 mm. Therefore, compared to previously reported PSRM performance, the steady-state error of the PSRM developed in this study is effectively reduced, which is significantly beneficial for positioning applications. The improved positioning performance can be mainly attributed to the following two factors: 1) the improved motor design effectively reduces the force ripple and deformation, and 2) the negative effects of friction are effectively eliminated by the control strategy based on nonlinear friction compensation. The experimental results reported here illustrate the promising precision positioning capability of the proposed PSRM.

The steady-state error of the PSRM mainly originates from the limited time and current available in practice, the limited resolution of the linear optical encoder, machining error, current and force ripples, and friction estimation error. Machining error, time and current limitations, and encoder resolution limitations are unavoidable in a PSRM, whereas the current and force ripples can be reduced by means of an improved motor design or an effective control strategy. By applying an

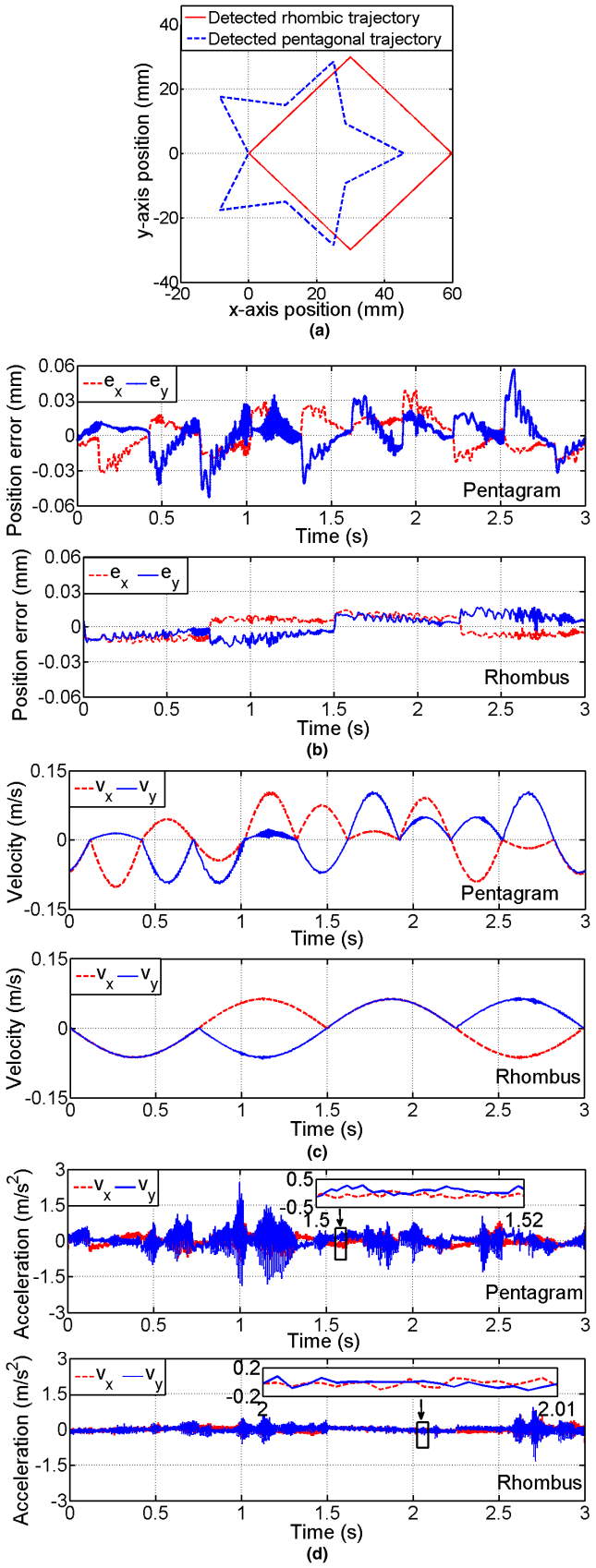

FIGURE 8. (a) Position trajectory, (b) position error, (c) velocity, and (d) acceleration for rhombic and pentagonal trajectory tracking.

effective control strategy or contactless bearings, the steady-state error caused by friction in a PSRM can be effectively eliminated.

V. CONCLUSION

This paper presented the design, control, and performance of a long-stroke PSRM for precision positioning applications. The proposed PSRM has a planar stroke of 170 mm × 290 mm. Its steady-state error for translational motion with a travel range of 290 mm is ±1.5 μm. The proposed control scheme was experimentally verified, as were the effectiveness of the developed precision long-stroke PSRM and its promise for application in precision positioning devices. In addition, the positioning performance of the PSRM could be effectively improved by using contactless bearings. To further facilitate the application of PSRMs for precision positioning, the development of a contact-free PSRM will be a significant focus of future work.

REFERENCES

[1] J. Lin, D. Zhao, M. Lu, and A. Yi, "Modeling and analysis of a novel decoupled vibration-assisted swing cutting system for micro/nano-machining surface," *IEEE Access*, vol. 6, pp. 70388–70396, 2018.

[2] M. Li, K. Yang, Y. Zhu, H. Mu, and C. Hu, "State/model-free variable-gain discrete sliding mode control for an ultraprecision wafer stage," *IEEE Trans. Ind. Electron.*, vol. 64, no. 8, pp. 6695–6705, Aug. 2017.

[3] V. H. Nguyen and W. J. Kim, "Design and control of a compact lightweight planar positioner moving over a concentrated-field magnet matrix," *IEEE/ASME Trans. Mechatronics*, vol. 18, no. 3, pp. 1090–1099, Jun. 2013.

[4] M. U. Khan, C. Prelle, F. Lamarque, and S. Büttgenbach, "Design and assessment of a micropositioning system driven by electromagnetic actuators," *IEEE/ASME Trans. Mechatronics*, vol. 22, no. 1, pp. 551–560, Feb. 2017.

[5] M.-Y. Chen, H.-H. Huang, and S.-K. Hung, "A new design of a submicropositioner utilizing electromagnetic actuators and flexure mechanism," *IEEE Trans. Ind. Electron.*, vol. 57, no. 1, pp. 96–106, Jan. 2010.

[6] Z. Wang, C. Hu, Y. Zhu, S. He, M. Zhang, and H. Mu, "Newton-ILC contouring error estimation and coordinated motion control for precision multiaxis systems with comparative experiments," *IEEE Trans. Ind. Electron.*, vol. 65, no. 2, pp. 1470–1480, Feb. 2018.

[7] F. F. M. El-Sousy and K. A. Abuhasel, "Adaptive nonlinear disturbance observer using double loop self-organizing recurrent wavelet-neural-network for two-axis motion control system," *IEEE Trans. Ind. Appl.*, vol. 54, no. 1, pp. 764–786, Jan./Feb. 2018.

[8] C. Li, C. Li, Z. Chen, and B. Yao, "Advanced synchronization control of a dual-linear-motor-driven gantry with rotational dynamics," *IEEE Trans. Ind. Electron.*, vol. 65, no. 9, pp. 7526–7535, Sep. 2018.

[9] G. Zhou, X. Huang, H. Jiang, and Z. Wang, "A novel ohmic-loss reduction control strategy for planar motor," *IEEE Trans. Magn.*, vol. 48, no. 11, pp. 2997–3000, Nov. 2012.

[10] J. Cao, S. Wang, Y. Zhu, and W. Yin, "Modeling the static vertical force of the core-type permanent-magnet planar motor," *IEEE Trans. Magn.*, vol. 44, no. 12, pp. 4653–4658, Dec. 2008.

[11] Y. Zhu, D. Yuan, M. Zhang, F. Liu, and C. Hu, "Unified wrench model of an ironless permanent magnet planar motor with 2D periodic magnetic field," *IET Elect. Power Appl.*, vol. 12, no. 3, pp. 423–430, Mar. 2018.

[12] S. Zhang, X. Dang, K. Wang, J. Huang, J. Yang, and G. Zhang, "An analytical approach to determine coil thickness for magnetically levitated planar motors," *IEEE/ASME Trans. Mechatronics*, vol. 22, no. 1, pp. 572–580, Feb. 2017.

[13] J. Pan, N. C. Cheung, and J. Yang, "High-precision position control of a novel planar switched reluctance motor," *IEEE Trans. Ind. Electron.*, vol. 52, no. 6, pp. 1644–1652, Dec. 2005.

[14] L. Zhang, B. Kou, L. Li, and B. Zhao, "Modeling and design of an integrated winding synchronous permanent magnet planar motor," *IEEE Trans. Plasma Sci.*, vol. 41, no. 5, pp. 1214–1219, May 2013.
[15] B. A. Sawyer, "Magnetic positioning device," U.S. Patent 3 376 578 A, Apr. 2, 1968.
[16] H.-J. Hu *et al.*, "Design and analysis of a planar flux-switching permanent magnet motor," *IEEE Trans. Magn.*, vol. 54, no. 11, Nov. 2018, Art. no. 8205606.
[17] N. Fujii and M. Fujitake, "Two-dimensional drive characteristics by circular-shaped motor," *IEEE Trans. Ind. Appl.*, vol. 35, no. 4, pp. 803–809, Jul./Aug. 1999.
[18] F. Treviso, M. A. Da Silveira, A. F. F. Filho, and D. Dorrell, "An induction planar actuator for surface inspection," *IEEE Trans. Magn.*, vol. 51, no. 11, Nov. 2015, Art. no. 8208004.
[19] K. S. Jung and Y. S. Baek, "Study on a novel contact-free planar system using direct drive DC coils and permanent magnets," *IEEE/ASME Trans. Mechatronics*, vol. 7, no. 1, pp. 35–43, Mar. 2002.
[20] B. Kou, H. Zhang, and L. Li, "Analysis and design of a novel 3-DOF Lorentz-force-driven DC planar motor," *IEEE Trans. Magn.*, vol. 47, no. 8, pp. 2118–2126, Aug. 2011.
[21] S.-D. Huang *et al.*, "Maximum-force-per-ampere strategy of current distribution for efficiency improvement in planar switched reluctance motors," *IEEE Trans. Ind. Electron.*, vol. 63, no. 3, pp. 1665–1675, Mar. 2016.
[22] G.-Z. Cao, L.-L. Li, S.-D. Huang, L.-M. Li, Q.-Q. Qian, and J.-A. Duan, "Nonlinear modeling of electromagnetic forces for the planar-switched reluctance motor," *IEEE Trans. Magn.*, vol. 51, no. 11, Nov. 2015, Art. no. 206605.
[23] S. D. Huang, G. Z. Cao, Z. Y. He, J. F. Pan, J. A. Duan, and Q. Q. Qian, "Nonlinear modeling of the inverse force function for the planar switched reluctance motor using sparse least squares support vector machines," *IEEE Trans. Ind. Informat.*, vol. 11, no. 3, pp. 591–600, Jun. 2015.
[24] F. Wang, C. Liang, Y. Tian, X. Zhao, and D. Zhang, "A flexure-based kinematically decoupled micropositioning stage with a centimeter range dedicated to micro/nano manufacturing," *IEEE/ASME Trans. Mechatronics*, vol. 21, no. 2, pp. 1055–1062, Apr. 2016.
[25] J. M. M. Rovers, J. W. Jansen, J. C. Compter, and E. A. Lomonova, "Analysis method of the dynamic force and torque distribution in the magnet array of a commutated magnetically levitated planar actuator," *IEEE Trans. Ind. Electron.*, vol. 59, no. 5, pp. 2157–2166, May 2012.
[26] T. Hu and W.-J. Kim, "Extended range six-DOF high-precision positioner for wafer processing," *IEEE/ASME Trans. Mechatronics*, vol. 11, no. 6, pp. 682–689, Dec. 2006.
[27] (2018). *H2W Technologies*. [Online]. Available: https://www.h2wtech.com/category/dual-axis-linear stepper#productInfo1
[28] (2018). *Planar Motor Incorporated*. [Online]. Available: http://www.planarmotor.com/ videos.html
[29] H. Zhu, T. J. Teo, and C. K. Pang, "Design and modeling of a six-degree-of-freedom magnetically levitated positioner using square coils and 1-D Halbach arrays," *IEEE Trans. Ind. Electron.*, vol. 64, no. 1, pp. 440–450, Jan. 2017.
[30] J. F. Pan and N. C. Cheung, "An adaptive controller for the novel planar switched reluctance motor," *IET Electr. Power Appl.*, vol. 5, no. 9, pp. 677–683, Nov. 2011.
[31] L. C. Dulger, M. T. Das, R. Halicioglu, S. Kapucu, and M. Topalbekiroglu, "Robotics and servo press control applications: Experimental implementations," in *Proc. Int. Conf. Control, Decis. Inf. Technol. (CoDIT)*, St. Julian's, Malta, Apr. 2016, pp. 102–107.
[32] R. Halicioglu, L. C. Dulger, and A. T. Bozdana, "An automation system for data processing and motion generation," in *Proc. Int. Artif. Intell. Data Process. Symp.*, Malatya, Turkey, Sep. 2017, pp. 1–9.
[33] C. C. de Wit, H. Olsson, K. J. Åström, and P. Lischinsky, "A new model for control of systems with friction," *IEEE Trans. Autom. Control*, vol. 40, no. 3, pp. 419–425, Mar. 1995.
[34] J. Yao, W. Deng, and Z. Jiao, "Adaptive control of hydraulic actuators with LuGre model-based friction compensation," *IEEE Trans. Ind. Electron.*, vol. 62, no. 10, pp. 6469–6477, Oct. 2015.
[35] G. Baoming, A. T. D. Almeida, and F. J. T. E. Ferreira, "Design of transverse flux linear switched reluctance motor," *IEEE Trans. Magn.*, vol. 45, no. 1, pp. 113–119, Jan. 2009.
[36] R. Krishnan, *Switched Reluctance Motor Drives: Modeling, Simulation, Analysis, Design, and Application*. Boca Raton, FL, USA: CRC Press, 2001, pp. 79–84.
[37] J. G. Amoros and P. Andrada, "Sensitivity analysis of geometrical parameters on a double-sided linear switched reluctance motor," *IEEE Trans. Ind. Electron.*, vol. 57, no. 1, pp. 311–319, Jan. 2010.

SU-DAN HUANG (M'17) received the B.Sc. and M.Sc. degrees in control theory and control engineering from Shenzhen University, Shenzhen, China, in 2009 and 2012, respectively, and the Ph.D. degree in electrical engineering from Southwest Jiaotong University, Chengdu, China, in 2016.

She is currently an Assistant Professor with the Shenzhen Key Laboratory of Electromagnetic Control, College of Mechatronics and Control Engineering, Shenzhen University. Her research interests include the design and control of planar switched reluctance motors, magnetic levitation systems, and control theory and its applications.

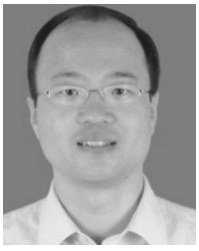

GUANG-ZHONG CAO (M'15–SM'17) received the B.Sc., M.Sc., and Ph.D. degrees in electrical engineering and automation from Xi'an Jiaotong University, Xi'an, China, in 1989, 1992, and 1996, respectively.

He is currently a Professor and the Director of the Shenzhen Key Laboratory of Electromagnetic Control, College of Mechatronics and Control Engineering, Shenzhen University, China. He has authored more than 100 articles in refereed journals and conference proceedings. His research interests include control theory, motor control, robotics, and the Internet of Things.

YEPING PENG (M'18) received the B.Sc. degree in mechanical design, manufacture, and automation from Harbin Engineering University, Harbin, China, in 2011, and the M.Sc. and Ph.D. degrees in mechanical engineering from Xi'an Jiaotong University, Xi'an, China, in 2014 and 2017, respectively.

She is currently an Assistant Professor with the Shenzhen Key Laboratory of Electromagnetic Control, College of Mechatronics and Control Engineering, Shenzhen University, China. Her main research interests include machine vision, image processing, and signal processing.

CHAO WU received the B.Sc. and M.Sc. degrees from Southwest Jiaotong University, Chengdu, China, in 2003 and 2006, respectively, and the Ph.D. degree in electrical engineering from Tsinghua University, Beijing, China, in 2010.

She is currently an Associate Professor with the Shenzhen Key Laboratory of Electromagnetic Control, College of Mechatronics and Control Engineering, Shenzhen University, China. Her research interests include power system dynamic analysis and control, and signal processing.

DELIANG LIANG (SM'13) received the B.S., M.S., and Ph.D. degrees in electrical engineering from Xi'an Jiaotong University, Xi'an, China, in 1989, 1992, and 1996, respectively.

From 2001 to 2002, he was a Visiting Scholar with the Science Solution International Laboratory, Tokyo, Japan. Since 1999, he has been with the Department of Electrical Engineering, Xi'an Jiaotong University, where he is currently a Professor. His current research interests include optimal design, control, and simulation of electrical machines, and electrical machine technology in renewable energy.

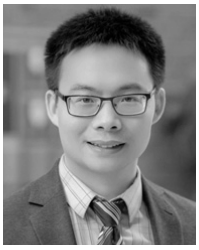

JIANGBIAO HE (S'08–M'15–SM'16) received the Ph.D. degree in electrical engineering with an emphasis on power energy conversion from Marquette University, Milwaukee, WI, USA, in 2015.

He is currently an Assistant Professor with the Department of Electrical and Computer Engineering, University of Kentucky, USA. He previously worked in industry, most recently as a Lead Engineer with GE Global Research, Niskayuna, NY, USA. He was with Eaton Corporate Research and Technology and Rockwell Automation before he joined GE in 2015. He has authored or co-authored more than 50 technical papers and 10 patent applications in power electronics and motor drives areas. His research interests include high-power high-frequency propulsion drives for electric transportation, renewable energy power conversion, and fault-tolerant operation of power conversion systems for safety-critical applications.

Dr. He has served as the Secretary of the Standards Sub-Committee for the IEEE Industrial Drives Group and an Organizing Committee Member of several large international conferences, including ECCE-2018, IEMDC-2019, and ITEC-2019. He has also served as an Associate Editor for several prestigious IEEE journals in electric power area.